

A multiscale study of film thickness dependent femtosecond laser spallation and ablation

Pengfei Ji and Yuwen Zhang

Department of Mechanical and Aerospace Engineering

University of Missouri

Columbia, MO 65211, USA

Abstract

Ab initio quantum mechanics, classical molecular dynamics and two-temperature model integrated multiscale simulation is carried out to study the film thickness dependent the femtosecond laser heating of silver. As an interval of 130.7296 nm , five silver films with increasing thickness from 392.1888 nm to 915.1072 nm are simulated. The absorbed laser fluence of 0.1 J/cm^2 and 0.3 J/cm^2 are chosen to observe the laser spallation and ablation. The simulation results show that film thickness has close correlation with the Kelvin degree of heating of the laser irradiated silver films, which further affects the laser spallation and ablation. Thicker film prolongs the time cost of the laser induced compressive thermal stress propagating through silver film and the rear surface reflection of compressive thermal stress into tensile thermal stress, which delays the tensile stress spallation. Suggestions for precise micromachining are proposed in this paper.

Keywords: laser ablation; laser spallation; micromachining; multiscale modeling; metal film.

Nomenclature

A	material constants describing the electron-electron scattering rate, $s^{-1}K^{-2}$
B	material constants describing the electron-phonon scattering rate, $s^{-1}K^{-1}$
C_e	electron heat capacity, $J/(m^3K)$
E	energy, J
f	Fermi-Dirac distribution function
g	electron density of states
G_{e-ph}	electron-phonon coupling factor, $W/(m^3K)$
J_{abs}	absorbed laser fluence, J/cm^2
k_e	electron thermal conductivity, $W/(mK)$
k_B	Boltzmann constant, $1.38 \times 10^{-23}J/K$
m	mass, kg
L	penetrating depth, m
\mathbf{r}_i	position of an atom
t	time, s
T	temperature, K
v	velocity, m/s
V_c	Volume of unit cell, m^3

Greek Letters

ε	electron energy level, J
μ	chemical potential, J
$\lambda\langle\omega^2\rangle$	second moment of the electron-phonon spectral function, meV^2
ρ	density, kg/m^3
τ_e	total electron scattering time
τ_{xx}	thermal stress, GPa

Subscripts and Superscripts

e	electron
F	Fermi
l	lattice
op	optical
p	pulse

1. Introduction

Owing to the unique merit of little collateral damage [1,2], femtosecond laser pulse processing of material has the advantage over conventional laser machining, which makes it as a widely acknowledged approach in micromachining and microfabrication [3–5]. With the miniaturization of the objective material to nanoscale, plenty of challenges to the conventionally macroscopic heat transfer theories come up [6–9]. Properly setting up the parameters of laser pulse and studying the optical, mechanical and thermophysical properties of material, help to achieve smoothly manufactured surface and highly precise control in femtosecond laser processing of thin silver film. When the laser pulse duration is comparable to the timescales of ultrafast laser irradiation induced thermal and mechanical response, the factors leading to laser spallation and ablation become complex.

Considerable attentions have been drawn in studying the ultrafast laser interaction with metal film. When the laser pulse duration is in the time scale shorter than picosecond, the nonequilibrium state between the laser excited hot electron subsystem and the cold lattice subsystem is significant, which cannot be solved by using the classical heat transfer methods and models [10]. Therefore, the two-temperature model was proposed to describe the nonequilibrium state [11]. The rapid melting and resolidification of gold film was simulated by combining the two-temperature model with the interfacial tracking method [12]. The effects of laser pulse width and fluence were studied [13]. Subsequently, by imposing the single pulse, multiple pulse and pulse train, Huang *et al.* carried out numerical simulations to investigate the effects of film thickness on laser melting and vaporization [14]. The morphology evolution of silver films with thickness from 2 nm to 20 nm deposited by using nanosecond laser pulse, was investigated by Hrishna *et al.* [15]. The effect of chromium film thickness on laser irradiated surface morphology was studied by Kim *et al.* [16], who found that there were greater hydrodynamic flow and recoil press for the 500 nm film than that of the 200 nm film. The one-dimensional and two-dimensional gold thin film gratings were fabricated with the help of nanosecond laser induced thermos-elastic force to detach the film from substrate [17].

There were a bunch of mechanisms interpreting the ultrafast laser spallation and ablation. The thermal mechanism stated that the high rate of vaporization of thermalized material and

formation of plasma induced the removal of laser irradiated material [18–20]. The mechanical mechanism explained that the removal of material resulted from the generation of tensile stress [21,22]. The Coulomb explosion mechanism couples the laser excited electronic energy from intense electromagnetic fields into atomic motion, which leads to the metal film explodes into plasma of ionized atoms [23–25]. The hot-electron blast force mechanism, which said that due to the nonequilibrium heated electronic regions from the optical penetration of the laser energy, the abrupt increase of electronic pressure exerts on the surface of the metal lattices and leads to the removal of the lattices [26–29]. Nevertheless, the mechanisms responsible for metal film thickness dependent femtosecond laser spallation and ablation are still open. The film thickness determines the available depth of thermal diffusion of the deposited laser energy [30], overall degree of heating and damping of the thermal stress induced by femtosecond laser pulse.

In this paper, a multiscale framework integrating the quantum mechanics (QM), molecular dynamics (MD) and two-temperature model (TTM), which was constructed in our previous work [31–35], is to be employed to fulfill the simulation of femtosecond laser spallation and ablation of the silver film. A database containing the electron temperature T_e dependent electron heat capacity C_e [32,35], electron thermal conductivity k_e [34] and effective electron-phonon coupling factor G_{e-ph} [31,35], is established from *ab initio* QM calculation, which are essential parameters in the MD and TTM simulations and ensure the overall accuracy of the simulation. The absorption of laser energy and thermal excitation of the electron subsystem is represented by the TTM. The spallation and ablation of silver film is observed from the atomic motion of silver atoms from MD simulation. Besides the original interatomic force in MD, an additional force acting on the nuclei is modeled by taking the electron-phonon coupled heat transfer into account.

2. Simulation method

Five silver films with thicknesses of 392.1888 nm , 522.9184 nm , 653.6480 nm , 784.3776 nm and 915.1072 nm were simulated. Considering the femtosecond laser radius is in the length scale of micrometer, the computational domain was treated as one dimensional in the x -direction. The length (in the y -direction) and width (in the z -direction) were set as 4.0853 nm . A brief recall of the QM-MD-TTM integrated framework [31–35] is presented in this paper. The volumetric energy source S of the incident laser pulse at per unit time, is expressed in terms of the following equation, which obeys the temporal Gaussian distribution,

$$S(x, t) = \frac{0.94J_{abs}}{t_p L} \exp\left(-\frac{x}{L}\right) \exp\left[-2.77 \frac{(t-t_0)^2}{t_p^2}\right], \quad (1)$$

where t_p is the laser pulse duration, which denotes the full width at half maximum (FWHM) of the laser intensity. L equals the summation of 12 nm optical penetration depth L_{op} [36] and 56 nm ballistic energy transport depth L_{ba} [37]. t_0 is the temporal center point of laser pulse.

Before femtosecond laser irradiation, the silver film samples were initially prepared at room temperature 300 K for 10 ps . The first 5 ps canonical ensemble simulation was for the preparation of equilibrating the electron subsystem and the lattice subsystem at room temperature 300 K . The second 5 ps microcanonical ensemble simulation was for the verification of the thermal equilibrium. The QM-MD-TTM combined simulation started at 10 ps . t_p and t_0 were

set as 500 fs and 25 ps, respectively. Hence, it ensured that the 15 ps temporal gap between the ending point of microcanonical ensemble simulation and the central point t_0 , is much longer than the duration of laser pulse t_p . In other words, the incident laser pulse did not impact the initial preparation and verification processes. In this paper, the entire simulation lasted for 200 ps. By setting the absorbed laser fluence as 0.1 J/cm² and 0.3 J/cm², the femtosecond laser induced spallation and ablation were observed sequentially. Two empty spaces were left outside the front surface and the rear surface of the silver film, which allowed the ablated and spalled silver segments to fly away. In other words, the front surface of the silver film was set as 196.0944 nm from the zero point ($x = 0$ nm) and the end of the computational domain was set as 65.3648 nm from the rear surface of the silver film. The overall length of the computational domain varied with thicknesses of the five films. Free boundary conditions were applied on the two surfaces of the silver film, while period boundary conditions were applied on the surfaces perpendicular to y- and z- directions.

According to the TTM, due to the electron-electron scattering time is short than the electron-phonon scattering time, the laser energy is firstly absorbed by the electron [11]. The energy equation of the electron subsystem is expressed in

$$C_e \frac{\partial T_e}{\partial t} = \nabla(k_e \nabla T_e) - G_{e-ph}(T_e - T_l) + S(x, t), \quad (2)$$

where C_e , k_e and G_{e-ph} are to be determined from QM calculation by using the ABINIT package [38]. The finite difference method (FDM) is used to solve the evolution of the electron energy in Eq (2). The modeled mathematical expression for C_e , k_e and G_{e-ph} at given T_e are

$$\begin{cases} C_e|_{T_e} = \frac{1}{V_c} \int_{-\infty}^{\infty} \left(\frac{\partial g|_{T_e}}{\partial T_e} f|_{T_e} + g|_{T_e} \frac{\partial f|_{T_e}}{\partial T_e} \right) \varepsilon d\varepsilon \\ k_e|_{T_e} = \frac{1}{3V_c} v_F^2 \tau_e|_{T_e} \int_{-\infty}^{\infty} \left(\frac{\partial g|_{T_e}}{\partial T_e} f|_{T_e} + g|_{T_e} \frac{\partial f|_{T_e}}{\partial T_e} \right) \varepsilon d\varepsilon. \\ G_{e-ph}|_{T_e} = \frac{1}{V_c} \frac{\pi \hbar k_B \lambda \langle \omega^2 \rangle|_{T_e}}{g(\varepsilon_F)|_{T_e}} \int_{-\infty}^{\infty} g|_{T_e}^2 \left(-\frac{\partial f|_{T_e}}{\partial \varepsilon} \right) d\varepsilon \end{cases} \quad (3)$$

Under femtosecond laser excitation, $g|_{T_e}$, $g(\varepsilon_F)|_{T_e}$, $f|_{T_e}$ and $\lambda \langle \omega^2 \rangle|_{T_e}$ in Eq. (3) change with different T_e . g is the electron density of states (EDOS) and $g(\varepsilon_F)$ is the EDOS at Fermi level ε_F . f is the Fermi-Dirac distribution. $\lambda \langle \omega^2 \rangle$ is the second moment of electron-phonon spectral function, which contains the detailed information on the electron-phonon coupled heat transfer. V_c is the volume of unit cell. v_F is the Fermi velocity. τ_e denotes the total electron scattering time, which equals the $(AT_e^2 + BT_l)^{-1}$. $A = 3.57 \times 10^6 \text{ s}^{-1} \text{K}^{-2}$ and $B = 1.12 \times 10^{11} \text{ s}^{-1} \text{K}^{-1}$ are two material constants of silver [39,40]. \hbar and k_B are reduced Planck constant and Boltzmann constant, respectively. Finite temperature density functional theory (FT-DFT) was implemented in calculating $g|_{T_e}$, $g(\varepsilon_F)|_{T_e}$, $f|_{T_e}$ and $\lambda \langle \omega^2 \rangle|_{T_e}$. The valence electrons $4d^{10}5s^1$ was taken in FT-DFT calculation. The local density approximation (LDA) with a plane wave cutoff of 28 eV was adopted in computing the exchange and correlation energy. $10 \times 10 \times 10$ Monkhorst-Pack k -point grids were used to sample the Brillouin zone, which had been tested to meet the convergence. The finally calculated T_e dependent C_e , k_e and G_{e-ph} are plotted in Fig. 1. For the purposes of evaluating thermal diffusion in the electron subsystem and the time cost for the

thermal energy to be transported from the electron subsystem to the lattice subsystem (by decreasing 1 K of T_e), the thermal diffusivity α_e (ratio of k_e to C_e) and t_{e-ph} (ratio of C_e to G_{e-ph}) are plotted in Figs. 1(d) and 1(e) as well. More detailed analyses and discussions of the results in Fig. 1 will be presented in the subsequent section.

The electron-phonon coupled heat transfer results in an addition force acting on the nuclei. The equation of atomic motion in MD simulation is expressed in the following equation

$$m_i \frac{d^2 \mathbf{r}_i}{dt^2} = -\nabla U + \frac{E_{e-ph}}{\Delta t_{MD}} \frac{m_i \mathbf{v}_i^T}{\sum_{j=1}^{N_V} m_j (\mathbf{v}_j^T)^2}, \quad (4)$$

where m_i , \mathbf{r}_i and \mathbf{v}_i^T are the mass, position and thermal velocity of atom i , respectively. The interatomic force acting on the nuclei is $-\nabla U$. Here U is interatomic potential described by the embedded atom method (EAM), which was also fitted from QM approach [41]. N_V is the number atoms in each FMD cell. In each MD time step Δt_{MD} , the thermal energy E_{e-ph} transporting from the electron subsystem to the lattice subsystem is $\Delta t_{MD} \sum_{k=1}^{n_t} G_{e-ph} V_N (T_e^k - T_l) / n_t$, where n_t indicates the MD time step contains n_t times of FDM time step Δt_{FDM} . V_N is the volume of FDM cell. T_e^k is the average electron temperature of each computational cell per FDM time step. The QM-MD-TTM integrated framework is constructed by combing Eqs. (1)-(4). The simulation code is developed as an extension of the ABINIT package [38] and the TTM part in the IMD [42]. During the QM-MD-TTM integrated simulation, the time steps Δt_{MD} and Δt_{FDM} were set as 1 fs and 0.005 fs to meet the von Neumann stability criterion [43].

3. Results and discussion

3.1 Spallation triggered for $J_{abs} = 0.1\text{ J/cm}^2$

When J_{abs} was 0.1 J/cm^2 , thermal melting of the front surface and laser spallation of the rear surface were seen for the film with thickness of 392.1888 nm . Whereas, only thermal melting was found for the other four films. The occurrence of laser spallation was slower than the thermal melting. Thermal melting was found a few picoseconds after femtosecond laser irradiation, while the laser spallation was observed hundreds of picoseconds after laser pulse. It is concluded that thermal melting is an ultrafast process due to the strong electron-phonon coupled heat transfer. Laser spallation is a tardy process requiring accumulation of the tensile stress.

The temporal and spatial distribution of electron temperature T_e for cases with film thicknesses of 392.1888 nm , 653.6480 nm and 915.1072 nm are shown in Fig. 2(a), 2(b) and 2(c), respectively. The laser irradiated front surface of the silver film locates at $x = 196.0944\text{ nm}$. For the case with film thickness of 392.1888 nm , it can be seen in Fig. 2(a) that T_e elevates to $2,000\text{ K}$ (or more) throughout the silver film right after $t = 25\text{ ps}$, which indicates the depth of femtosecond laser heating of the electron subsystem is significantly greater than 392.1888 nm . When the film thickness is increased to 653.6480 nm , there is an obvious temperature difference between T_e at the rear surfaces of Fig. 1(a) and Fig. 1(b) right after $t = 25\text{ ps}$. Furthermore, when the film thickness is increased to 915.1072 nm , Figure 2(c) shows that T_e at the rear surface is not appreciably impacted by femtosecond incident laser heating from the front surface.

According to [44–46], thermal confinement is mathematically expressed as $t_p < \tau_{e,cond} = L^2/\alpha_e$. In this paper, by taking $\alpha_e = 6.202 \times 10^{-4} \text{ m}^2/\text{s}$ at $T_e = 10^4 \text{ K}$ (as shown in Fig. 1(d)) and $L = 68 \text{ nm}$ in Eq. (1), $\tau_{e,cond}$ is estimated as 7.458 ps . Considering the laser pulse duration is 500 fs , which is much short than the time $\tau_{e,cond}$ cost to dissipate the absorbed laser energy via electron heat conduction. As extrapolated from Fig. 1(d), the criterion of eliminating thermal confinement corresponds $\alpha_e = 9.248 \times 10^{-3} \text{ m}^2/\text{s}$, which requires $T_e < 2046.91 \text{ K}$. Therefore, thermal confinement exists in the shallow region below the front surface of the silver film to $\sim 457.5536 \text{ nm}$. The electron thermal diffusivity α_e calculated in Fig. 1(d) shows that at higher T_e , the capability of the electron subsystem to conduct the absorbed laser energy relative its capability to reserve the laser energy becomes weaker, which further enhances the thermal confinement. Moreover, at higher T_e , G_{e-ph} present increasing trend, which leads to the faster transfer rate of confined thermal energy from the electron subsystem to the lattice subsystem.

In addition, after femtosecond laser heating, the absorbed laser energy gradually transports from the electron subsystem to the lattice subsystem, which results in the decrease of T_e . Nevertheless, due to the thinnest film thickness in Fig. 2(a), $T_e \geq 2,000 \text{ K}$ at the front surface lasts from 25 ps to 60 ps . Whereas, in Fig. 2(b) and 2(c), $T_e \geq 2,000 \text{ K}$ at the front surface lasts from 25 ps to 42 ps . Moreover, in Fig. 2(b) and 2(c), the profiles of T_e decreasing from $T_e \geq 2,000 \text{ K}$ to temperature lower than $1,000 \text{ K}$ show the right half bell shape. As seen from Fig. 1(e), t_{e-ph} is smaller at lower T_e , which reveals the electron-phonon coupled heat transfer facilitates the decreasing of T_e becomes faster. Two splits are found at $\sim 170 \text{ ps}$ in Fig. 2(a). Since the two splits occur at the region far behind the laser heated front surface and T_e at the original points of these two points are smaller than that under the front surface, it is conjectured that the two splits are caused by mechanical reason, rather than the thermal reason.

The temporal and spatial distribution of lattice temperature T_l in Fig. 3 presents the detailed information on T_l evolution, which is resulted from the electron-phonon coupled heat transfer. At $t = 25 \text{ ps}$, even though the electron subsystem has been heated throughout the silver film (in Fig. 2), the majority part of the lattice still keep cold (in Fig. 3). Right after tens of picoseconds, the lattice subsystem is gradually heated. In Fig. 3(a), the lattice subsystem is heated greater than $1,007.12 \text{ K}$ after $t = 50 \text{ ps}$. However, owing to the sufficient thickness for the films in Fig. 3(b) and 3(c), the depths of heated lattice subsystem ($T_l > 1000 \text{ K}$) are limited to 150.3390 nm below the front surface of the silver film. It should be pointed out that there is a T_l decreased region ($145 \text{ ps} < t < 165 \text{ ps}$) near the rear surface of the silver film in Fig. 3(a). Right after the T_l decreased region disappears, the rear ($x = 475.8557 \text{ nm}$) split appears. However, for the other (front $x = 376.5012$) split in Fig. 3(a), T_l at its starting point is not seen obvious difference from its foregoing region. Therefore, the reason leading to these two splits remains open.

By observing the temporal and spatial distribution of normalized density ($\rho^* = \rho/\rho_0$, where $\rho_0 = 10.49 \text{ g/cm}^3$ is density of silver at room temperature) in Fig. 4, it can be found that the overall ρ^* in Fig. 4(a) is smaller than those in Figs. 4(b) and 4(c). Recalling the greater T_l seen in Fig. 3(a) than those in Figs. 3(b) and 3(c), the smaller ρ^* in Fig. 4(a) is concluded from the reason of larger magnitude of thermal expansion. Right upon laser heating, there are expanded regions ($\rho^* < 1$) generated near the front surface and rear surface of the silver film. Due to the degree of heating in the front surface is much greater than that of the rear surface, greater magnitude of thermal expansion is seen from the front surface. In addition, there is also compressed region ($\rho^* > 1$) generated from front surface and developing along x -direction into deeper side of the film. Because of the differences among the thicknesses of silver films in Fig.

4, time cost for the compressed regions travelling from the front surface to the rear surface are different.

In Fig. 4(a), right after the compressed regions travel to the rear surface at ~ 130 ps, it reflects back in terms of expanded regions traveling along the direction from the rear surface to the front surface. The expanded regions reflected from the rear surface collide with the expanded region generated from the front surface, which results in the split at position $x = 475.8557$ nm. Therefore, the T_l decreased regions found in Fig. 3(a) is because of the emergence of the expanded regions, which consumes the thermal energy to overcome interatomic attraction during expansion process. As for the other split at position $x = 376.5012$ nm in Fig. 4(a), it is not only because of the collision of the two expanded regions travelling along opposite direction, but also because of the front surface thermal expansion of the bulk silver film. Additionally, as seen in Fig. 4(a), the melting region shows a density band with uniform ρ^* below the front surface.

In order to get a deeper sight into the femtosecond laser heating induced thermal expansion and the two splits, the thermal stress τ_{xx} is computed and shown in Fig. 5. To provide agreements with contours in Figs. 2-4, only the proportion of silver with $\rho^* > 0.1$ is drawn in Fig. 5. The compressive τ_{xx} (in dark color with positive value) is generated upon femtosecond laser heating and travel deeper inside the silver film. Comparing Fig. 5 with Fig. 4, it can be seen that the compressive τ_{xx} corresponds to compressed regions. Whereas, the tensile τ_{xx} (in light color with negative value) corresponds to expanded regions. In Fig. 5(a), due to the throughout heating of the silver film and free boundary conditions applied on the front surface and rear surface, compressive τ_{xx} are generated at both front and rear surfaces and travel along opposite directions. However, for the cases in Fig. 5(b) and 5(c), compressive τ_{xx} are not evidently seen from the rear surfaces of the two films. With the propagation of the tensile τ_{xx} in Fig. 5, a pronounced decrease of T_l is found in Fig. 3, which was also observed for laser interaction with nickel and gold films [47,48]. Due to the starting points of the two splits present tensile τ_{xx} spalling the silver film, the splits belong to laser spallation. After the emergences of the two splits in Fig. 5(a), the tensile τ_{xx} reflects as compressive τ_{xx} . Each starting point of the split generates two sorts of compressive τ_{xx} traveling to the front surface and rear surface. Moreover, as shown in Fig. 5(a), the overlapping two compressive τ_{xx} forms greater compressive τ_{xx} when 184 ps $< t < 200$ ps.

The film thickness dependent laser melting depth L_{mel} for the cases with $J_{abs} = 0.1$ J/cm² are measured and listed in Table 1. The reference point of L_{mel} is taken as the initial location of the front surface (196.0944 nm) of the laser film. As seen in Table 1, L_{mel} decreases with the increase of film thickness. With the film thickness increases from 392.1888 nm to 522.9184 nm, the greatest decrease of melt depth is seen in Table 1. When the same amount of laser energies are deposited into the five silver films with different thickness, the thicker silver film will result in smaller Kelvin degree of laser heating. T_l at the melting boundary show values close to the reported melting point of silver 1234.93 K [49], which verifies the validity of the current QM-MD-TTM integrated simulation. During the 200 ps simulation, laser spallation is triggered only for the case with film thickness of 392.1888 nm. From the perspective of micromachining, when $J_{abs} = 0.1$ J/cm², for the silver film with thickness 392.1888 nm can be spalled with the steady surface left for the remained bulk film. As for the other four films, longer simulation still needs to be carried out to see whether the laser spallation will happen or not.

3.2 Coexistence of spallation and ablation triggered for $J_{abs} = 0.3 \text{ J/cm}^2$

When J_{abs} is 0.3 J/cm^2 , femtosecond laser induced spallation and ablation were seen for the cases with film thicknesses of 392.1888 nm and 522.9184 nm . Whereas, only ablation was seen for the other three cases with film thicknesses of 653.6480 nm , 784.3776 nm and 915.1072 nm .

The distributions of T_e for the cases with thicknesses of 392.1888 nm , 653.6480 nm and 915.1072 nm are plotted in Fig. 6(a), 6(b) and 6(c). Comparing with the T_e distribution for the cases in Fig. 2, it can be seen that the time cost for the high T_e to get cooled down is much longer in Fig. 6, owing to the larger amount of laser energy deposition into the silver film. Moreover, recalling t_{e-ph} calculated in Fig. 1(d), the greater T_e leads to longer time during the process of decreasing T_e by electron-phonon coupled heat transfer, which is another factor leading to the longer time cost for the cases in Fig. 6 than those in Fig. 2. At 27 ps of the cases in Fig. 6(a), 6(b) and 6(c), T_e at the rear surface of the silver film are 5071.58 K , 354.89 K and 303.01 K , respectively. Therefore, it can be concluded that even though the laser fluence increases, the silver film with thickness greater than 653.6480 nm is sufficient to keep the rear side of the film being not significantly heated. At 170 ps , the silver film in Fig. 6(a) has been totally split into several segments. It should be noted that T_e of these segments from the front surface to the rear surface range from $4,533.94 \text{ K}$ to 1693.15 K . Therefore, besides the discussed mechanical reason of laser spallation at lower temperatures, the mechanism leading to those hot splits remains open.

The distributions of T_l for the cases with $J_{abs} = 0.3 \text{ J/cm}^2$ are calculated and plotted in Fig. 7. With the increase of the film thickness, the depth of heated region changes a lot. T_l at 80 ps at $x = 457.5536 \text{ nm}$ for the three cases Fig. 7(a), 7(b) and 7(c) are $2,817.66 \text{ K}$, 1575.14 K and $1,579.81 \text{ K}$, respectively, which confirms that when the film thickness is greater than 653.6480 nm , the effect of film thickness for laser heating with $J_{abs} = 0.3 \text{ J/cm}^2$ is no longer a dominate factor. As seen in Fig. 7(b), a T_l line appears since 70 ps and develops to the deeper regions with the evolution of time. The T_l line will be discussed in detail from the density distribution in Fig. 8. With the continuous progress of simulation, T_l gradually becomes in consistent with T_e in Fig. 6. The splits generated front the front surfaces of the cases in Figs. 7(b) and 7(c) show values above boiling point 2435.15 K of silver [49]. Explosive boiling are found from the front surface when $25 \text{ ps} < t < 80 \text{ ps}$, which is verified by T_l show values greater than 0.9 times of the critical temperature $6,410.15 \text{ K}$ of silver [49]. Due to the limits to the current QM-MD-TTM simulation, the generation of plasma is not included in this paper.

The temporal and spatial distribution of normalized density ρ^* are seen in Fig. 8. Comparing with the ρ^* shown in Fig. 4, due to greater amount of laser energy deposition for the cases in Fig. 8, a wider compressed density wave band ($\rho^* > 1$) emerges. The upper boundary of the compressed density wave band is generated from the front surface of the silver film. The lower boundary of the compressed density wave band appears $\sim 130.7296 \text{ nm}$ below the upper boundary. For the case with thicker film, due to stronger resistance of stress of the unheated region near the rear surface, there are more compressed density seen Fig 8. Comparing Fig. 8(b) with Fig. 8(c), the lower boundary is clearer for the case with thicker film. It should be addressed that the higher fluence induces the faster compressed density wave propagating from the front surface to the rear surface, which advances the reflection of the compressed density wave to expanded density wave

($\rho^* < 1$). As seen at ~ 100 ps in Fig. 8(a) and ~ 152 ps in Fig. 8(b), after the reflection of compressed density wave, the thermal expansion of the rear surface becomes much faster. The faster expansion of the rear film may result in spallation of the silver beyond the 200 ps simulation of the current work. In addition, the melting boundary seen from ρ^* in Fig. 4(a) is not seen from ρ^* in Fig. 8(a), because the entire film with the thickness of 392.1888 nm has been melted. In Figs. 8(b) and 8(c), there are distinct boundaries dividing the melting region and solid region. Figure 8(a) presents the overall lower ρ^* than those in Figs. 8(b) and 8(c), which is because of smaller magnitudes of thermal expansion. The boundaries are also seen in the T_l distributions in Fig. 7(b) and 7(c). As aforementioned, the thicker silver film results in the smaller Kelvin degree of laser heating after the deposition of the same amount of laser energy, which further leads to partial melting of the two cases seen in Figs. 7(b) and 7(c).

Subsequent to the reflection of the compressed density wave into the expanded density wave, the laser spallation is triggered in tens of picosecond. As discussed in Figs. 4 and 5, the compressed density wave corresponds to the compressive τ_{xx} . The expanded density wave corresponds to the tensile τ_{xx} , which results in the spallation of the silver film. The temporal and spatial distribution of τ_{xx} for the cases with $J_{abs} = 0.3$ J/cm² are depicted in Fig. 9. The propagation of the compressive τ_{xx} from the front surface to the rear surface of the silver film in Fig. 9 agrees with propagation of the compressed density waves discussed in Fig. 8. It can be seen that the original points of those splits near the rear surface of the silver film have tensile τ_{xx} , which has been concluded as laser spallation. However, the original points of the splits seen below the front surface of the silver film possess compressive τ_{xx} . Since the material removal in laser spallation results from the tensile τ_{xx} , the compressive τ_{xx} of the splits near the front surface is not responsible for the removal process. Moreover, as seen from the T_l distributions in Fig. 8(b), before the occurrence of the splits, T_l is much higher than the boiling point 2435.15 K and even greater than the critical point 6,410.15 K of silver. Whereas, the ρ^* distribution show liquid and solid mixed phases, which demonstrates the laser heated region is superheated. Ultrafast thermal expansion of superheated region results in the outer region of the superheated silver being ablated firstly. As seen at 200 ps, all of the superheated silver finally gets ablated. Hence, the laser ablation is a thermal effect caused by the ultrafast heat accumulation and superheating of the ablated silver. Although the occurrence of spallation is not seen in the cases of Figs. 9(b) and 9(c), it is believed that spallation might happen by continuing the simulation after 200 ps. Calculation result of τ_{xx} shows that compressive τ_{xx} decreases with its propagation to the rear surface. Therefore, if the compressive τ_{xx} is not strong enough and the film is sufficient thick to damp the compressive τ_{xx} , the laser spallation will not happen. The other solution to prevent the occurrence of laser spallation is to absorb the compressive τ_{xx} when it arrives the rear surface of the silver film.

Table 2 presents the spallation depth L_{spa} and ablation depth L_{abl} for the cases with $J_{abs} = 0.3$ J/cm². With the increase of laser fluence from 0.1 J/cm² to 0.3 J/cm², stronger τ_{xx} is generated, which results in the faster propagation of τ_{xx} . Therefore, laser spallation is also seen for the film with thickness of 522.9184 nm during the 200 ps simulation time, which is not seen when $J_{abs} = 0.1$ J/cm². Once upon laser irradiation, the compressive τ_{xx} generated from the front surface propagates to the rear surface of the film. Due to the different film thicknesses, the time cost for the compressive thermal stresses traveling from the front surface to the rear surface are different. The time difference consequently determines the moment of reflected tensile stress

to spalls the silver film. The results in Table 2 indicates that when $J_{abs} = 0.3 \text{ J/cm}^2$, the laser spallation damages the silver films (with thicknesses of 392.1888 nm and 522.9184 nm) into a few small segments. For the silver film without laser spallation, steady surface is seen from the front side of the remained silver film. As aforementioned, if the laser spallation is prohibited by weakening the compressive τ_{xx} under high laser fluence irradiation, it will leave the only happening of laser ablation. Thereby, to properly impose external condition to reduce the compressive τ_{xx} propagating to the rear surface, the precise micromachining of silver film laser ablation can be realized.

4. Conclusion

The dependence of film thickness on femtosecond laser spallation and ablation has been investigated in this paper. The simulation takes advantages of the highly accurate QM determination of the electron thermophysical properties, the detailed description of the laser pulse induced atomic motion and phase change process, as well as the inclusion of energy evolution of the laser energy excited electron subsystem in continuum. When $J_{abs} = 0.1 \text{ J/cm}^2$, spallation takes place for the film of 392.1888 nm, which is not seen for the other four films. Ablation is observed when $J_{abs} = 0.3 \text{ J/cm}^2$. It is concluded that laser spallation is induced by the mechanical mechanism of the tensile τ_{xx} . On the contrary, laser ablation happens at much higher T_l than that of laser spallation and is limited to the laser heated region under the front surface. Due to the laser spallation needs long time for the compressive τ_{xx} travelling throughout the film as prerequisite, the laser ablation is triggered earlier than laser spallation. For the thicker film, the longer lagging behavior of laser spallation. The coexistence of ablation and laser spallation results in the damage of the silver film into several small segments. From the perspective of improving the quality of micromachining, to properly choose the thinner silver film enables spallation from the rear surface and keeps melting at the front surface of low laser fluence heating. While under high laser fluence, it is suggested to weaken the compressive τ_{xx} before its reflection at the rear surface and leave only ablation happening at the front surface of the silver film.

Acknowledgement

Support for this work by the U.S. National Science Foundation under grant number CBET-133611 is gratefully acknowledged.

References

- [1] Stuart et al. (1996) Nanosecond-to-Femtosecond Laser-Induced Breakdown in Dielectrics, *Phys. Rev. B*, **53**(4), pp. 1749–1761.
- [2] Sudrie et al. (2002), Femtosecond Laser-Induced Damage and Filamentary Propagation in Fused Silica., *Phys. Rev. Lett.*, **89**(18), p. 186601.
- [3] Gattass, R. R., and Mazur, E., (2008) Femtosecond Laser Micromachining in Transparent Materials, *Nat. Photonics*, **2**(4), pp. 219–225.
- [4] Ramanathan, D., and Molian, P. A., (2002) Micro- and Sub-Micromachining of Type IIa Single Crystal Diamond Using a Ti:Sapphire Femtosecond Laser, *J. Manuf. Sci. Eng.*,

124(2), p. 389.

- [5] Stoian et al. (2002) Surface Charging and Impulsive Ion Ejection during Ultrashort Pulsed Laser Ablation,” *Phys. Rev. Lett.*, **88**(9), p. 97603.
- [6] Cahill et al. (2003) Nanoscale Thermal Transport, *J. Appl. Phys.*, **93**(2), p. 793.
- [7] Cahill et al. (2014) Nanoscale Thermal Transport. II. 2003–2012,” *Appl. Phys. Rev.*, **1**(1), p. 11305.
- [8] Ji, P., and Zhang, Y., (2013) First-Principles Molecular Dynamics Investigation of the Atomic-Scale Energy Transport: From Heat Conduction to Thermal Radiation,” *Int. J. Heat Mass Transf.*, **60**(1), pp. 69–80.
- [9] Ji et al. (2013) Structural, Dynamic, and Vibrational Properties during Heat Transfer in Si/Ge Superlattices: A Car-Parrinello Molecular Dynamics Study, *J. Appl. Phys.*, **114**(23), p. 234905.
- [10] Ji, P., and Zhang, Y., (2013) Femtosecond Laser Processing of Germanium: An Ab Initio Molecular Dynamics Study, *J. Phys. D: Appl. Phys.*, **46**, p. 495108.
- [11] Anisimov et al. (1974) Electron Emission from Metal Surfaces Exposed to Ultrashort Laser Pulses, *J. Exp. Theor. Phys.*, **39**(2), pp. 375–377.
- [12] Zhang, Y., and Chen, J. K., (2008) An Interfacial Tracking Method for Ultrashort Pulse Laser Melting and Resolidification of a Thin Metal Film,” *J. Heat Transfer*, **130**(6), p. 62401.
- [13] Huang, J et al. (2009) Ultrafast Solid–liquid–vapor Phase Change of a Gold Film Induced by Pico- to Femtosecond Lasers,” *Appl. Phys. A*, **95**(3), pp. 643–653.
- [14] Huang, J et al. (2010) Ultrafast Phase Change During Femtosecond Laser Interaction with Gold Films: Effect of Film Thickness,” *Numer. Heat Transf. Part A Appl.*, **57**(12), pp. 893–910.
- [15] Krishna et al. (2010) Thickness-Dependent Spontaneous Dewetting Morphology of Ultrathin Ag Films,” *Nanotechnology*, **21**(15), p. 155601.
- [16] Kim, J., and Na, S., (2007) Metal Thin Film Ablation with Femtosecond Pulsed Laser,” *Opt. Laser Technol.*, **39**(7), pp. 1443–1448.
- [17] Shin et al. (2010) Fabrication of Au Thin Film Gratings by Pulsed Laser Interference, *Appl. Surf. Sci.*, **256**(9), pp. 2944–2947.
- [18] Ren et al. (2013) Thermal Ablation of Metal Films by Femtosecond Laser Bursts,” *Int. J. Therm. Sci.*, **70**, pp. 32–40.
- [19] Schmidt et al. (2014) Understanding Thin Film Laser Ablation: The Role of the Effective Penetration Depth and the Film Thickness, *Phys. Procedia*, **56**, pp. 1007–1014.
- [20] Sands et al. (1999) Evidence for a Thermal Mechanism in Excimer Laser Ablation of Thin

- Film ZnS on Si, J. Appl. Phys., **85**(7), p. 3855.
- [21] Toth et al. (1999) Pulsed Laser Ablation Mechanisms of Thin Metal Films, *Proc. SPIE 3822, Computer-Controlled Microshaping*, pp. 18–26.
 - [22] Demaske et al. (2010) Ablation and Spallation of Gold Films Irradiated by Ultrashort Laser Pulses, *Phys. Rev. B*, **82**(6), pp. 1–5.
 - [23] Li et al. (2015) Possible Evidence of Coulomb Explosion in the Femtosecond Laser Ablation of Metal at Low Laser Fluence, *Appl. Surf. Sci.*, **355**, pp. 681–685.
 - [24] Lin et al. (2012) A Coulomb Explosion Theoretical Model of Femtosecond Laser Ablation Materials, *Sci. China Technol. Sci.*, **55**(3), pp. 694–701.
 - [25] Stoian et al. (2000) Coulomb Explosion in Ultrashort Pulsed Laser Ablation of Al₂O₃, *Phys. Rev. B*, **62**(19), pp. 13167–13173.
 - [26] Tzou et al. (2002) Hot-Electron Blast Induced by Ultrashort-Pulsed Lasers in Layered Media, *Int. J. Heat Mass Transf.*, **45**(16), pp. 3369–3382.
 - [27] Tzou et al. (2005) Recent Development of Ultrafast Thermoelasticity, *J. Therm. Stress.*, **28**(6–7), pp. 563–594.
 - [28] Chen et al. (2006) A Semiclassical Two-Temperature Model for Ultrafast Laser Heating, *Int. J. Heat Mass Transf.*, **49**(1–2), pp. 307–316.
 - [29] Zhang et al. (2009) Micro- and Nanoscale Heat Transfer in Femtosecond Laser Processing of Metals, *High-Power and Femtosecond Lasers: Properties, Materials and Applications*, Nova Science Publishers, Inc., pp. 159–206.
 - [30] Matthias et al. (1994) The Influence of Thermal-Diffusion on Laser-Ablation of Metal-Films,” *Appl. Phys. a-Materials Sci. Process.*, **58**(2), pp. 129–136.
 - [31] Ji, P., and Zhang, Y., (2016) Ab Initio Determination of Effective Electron–phonon Coupling Factor in Copper, *Phys. Lett. A*, **380**(17), pp. 1551–1555.
 - [32] Ji, P., and Zhang, Y., (2016) Continuum-Atomistic Simulation of Picosecond Laser Heating of Copper with Electron Heat Capacity from Ab Initio Calculation, *Chem. Phys. Lett.*, **648**, pp. 109–113.
 - [33] Ji, P., and Zhang, Y., (2017) Melting , Ablation and Explosive Boiling of a Silver Film Induced by Femtosecond Laser Heating : A Multiscale Modeling Approach,” Submitted, pp. 1–36.
 - [34] Ji, P., and Zhang, Y., (2017) Multiscale Modeling of Femtosecond Laser Irradiation on Copper Film with Electron Thermal Conductivity from Ab Initio Calculation, *Numer. Heat Transf. Part A Appl.*, **71**(2), pp. 128–136.
 - [35] Ji, P., and Zhang, Y., (2017) Electron–Phonon Coupled Heat Transfer and Thermal Response Induced by Femtosecond Laser Heating of Gold, *J. Heat Transfer*, **139**(5), pp. 52001–52006.

- [36] Bäuerle, D., 2011, *Laser Processing and Chemistry*.
- [37] Ashcroft, N. W., and Mermin, N. D., (1976) Solid State Physics, Holt, Rinehart and Winston.
- [38] Gonze et al. (2009) ABINIT: First-Principles Approach to Material and Nanosystem Properties, *Comput. Phys. Commun.*, **180**(12), pp. 2582–2615.
- [39] Groeneveld et al. (1995) Femtosecond Spectroscopy of Electron-Electron and Electron-Phonon Energy Relaxation in Ag and Au, *Phys. Rev. B*, **51**(17), pp. 11433–11445.
- [40] Mills, K. C. et al. (1996) Thermal Conductivities of Molten Metals: Part 1 Pure Metals, *Int. Mater. Rev.*, **41**(6), pp. 209–242.
- [41] Sheng et al. (2011) Highly Optimized Embedded-Atom-Method Potentials for Fourteen FCC Metals, *Phys. Rev. B*, **83**(13).
- [42] Stadler et al. (1997) IMD: A Software Package for Molecular Dynamics Studies on Parallel Computers, *Int. J. Mod. Phys. C*, **8**(5), pp. 1131–1140.
- [43] Chant, T. F., (1984) For The Adevection Diffusion Equation, *SIAM J. Numer. Anal.*, **21**(2), pp. 272–284.
- [44] Jacques, S. L., (1993) Role of Tissue Optics and Pulse Duration on Tissue Effects during High-Power Laser Irradiation., *Appl. Opt.*, **32**(13), pp. 2447–2454.
- [45] Zhigilei et al. (1997) Molecular Dynamics Model for Laser Ablation and Desorption of Organic Solids, *J. Phys. Chem. B*, **101**(11), pp. 2028–2037.
- [46] Zhigilei, L. V., and Garrison, B. J., (2000) Microscopic Mechanisms of Laser Ablation of Organic Solids in the Thermal and Stress Confinement Irradiation Regimes, *J. Appl. Phys.*, **88**(3), pp. 1281–1298.
- [47] Ivanov, D. S., and Zhigilei, L. V, (2003) Effect of Pressure Relaxation on the Mechanisms of Short-Pulse Laser Melting., *Phys. Rev. Lett.*, **91**(10), p. 105701.
- [48] Leveugle et al. (2004) Photomechanical Spallation of Molecular and Metal Targets: Molecular Dynamics Study, *Appl. Phys. A Mater. Sci. Process.*, **79**(7), pp. 1643–1655.
- [49] Haynes, W. M., (2016) Melting , Boiling , Triple , and Critical Points of the Elements, *CRC Handbook of Chemistry and Physics, 97th Edition, 2016*, pp. 4-116-4–118.

Table 1 Film thickness dependent melting depth L_{mel} , T_l at the melting boundary and spallation depth L_{spa} for $J_{abs} = 0.1 \text{ J/cm}^2$

Film Thickness (nm)	L_{mel} (nm)	T_l (K) (at L_{mel})	L_{spa} (nm)
392.1888	111.1202	1205.65	183.0214
522.9184	84.9742	1183.88	N/A
653.6480	71.9013	1256.67	N/A
784.3776	75.1692	1238.80	N/A
915.1072	62.0966	1239.27	N/A

Table 2 Film thickness dependent spallation depth L_{spa} and ablation depth L_{abl} for $J_{abs} = 0.3 \text{ J/cm}^2$.

Film Thickness (nm)	L_{spa} (nm)	L_{abl} (nm)
392.1888	451.0171	261.4592
522.9184	535.9914	210.8015
653.6480	N/A	137.2661
784.3776	N/A	133.9978
915.1072	N/A	130.7296

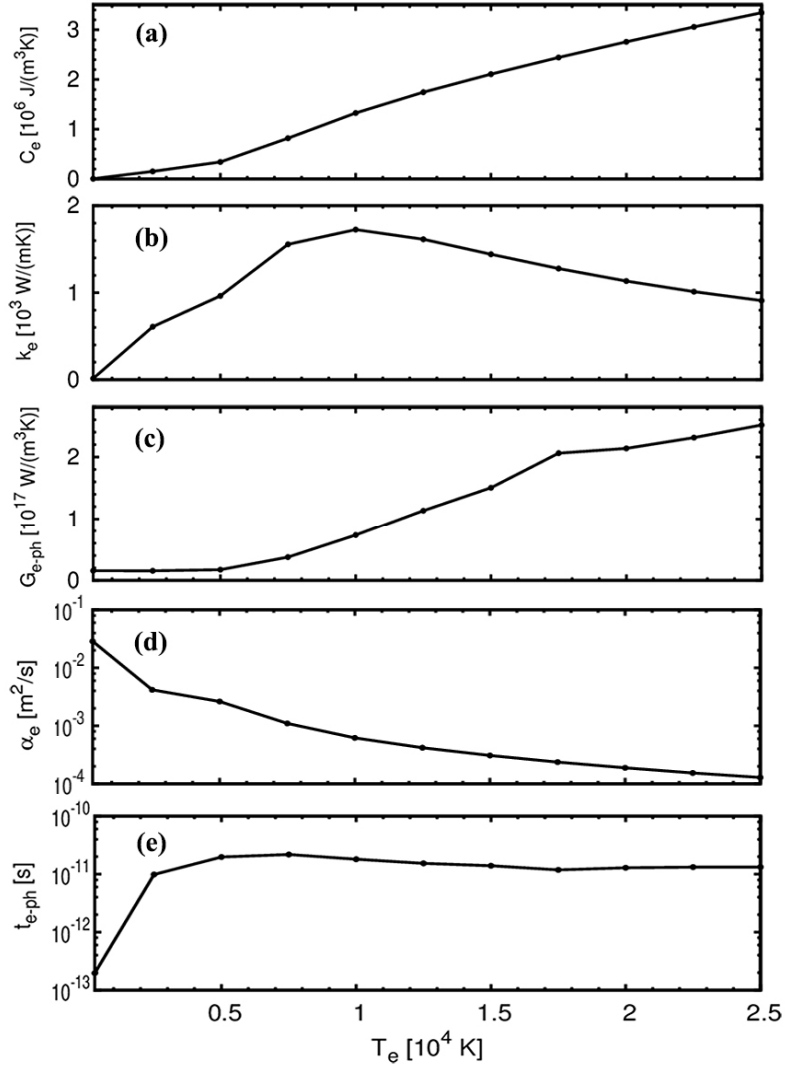


Fig.1 Electron temperature T_e dependent (a) electron heat capacity C_e , (b) electron thermal conductivity k_e , (c) effective electron-phonon coupling factor G_{e-ph} , (d) electron thermal diffusivity α_e and (e) time cost t_{e-ph} for the laser energy to be transferred from the electron subsystem to the lattice subsystem by decreasing T_e of 1K.

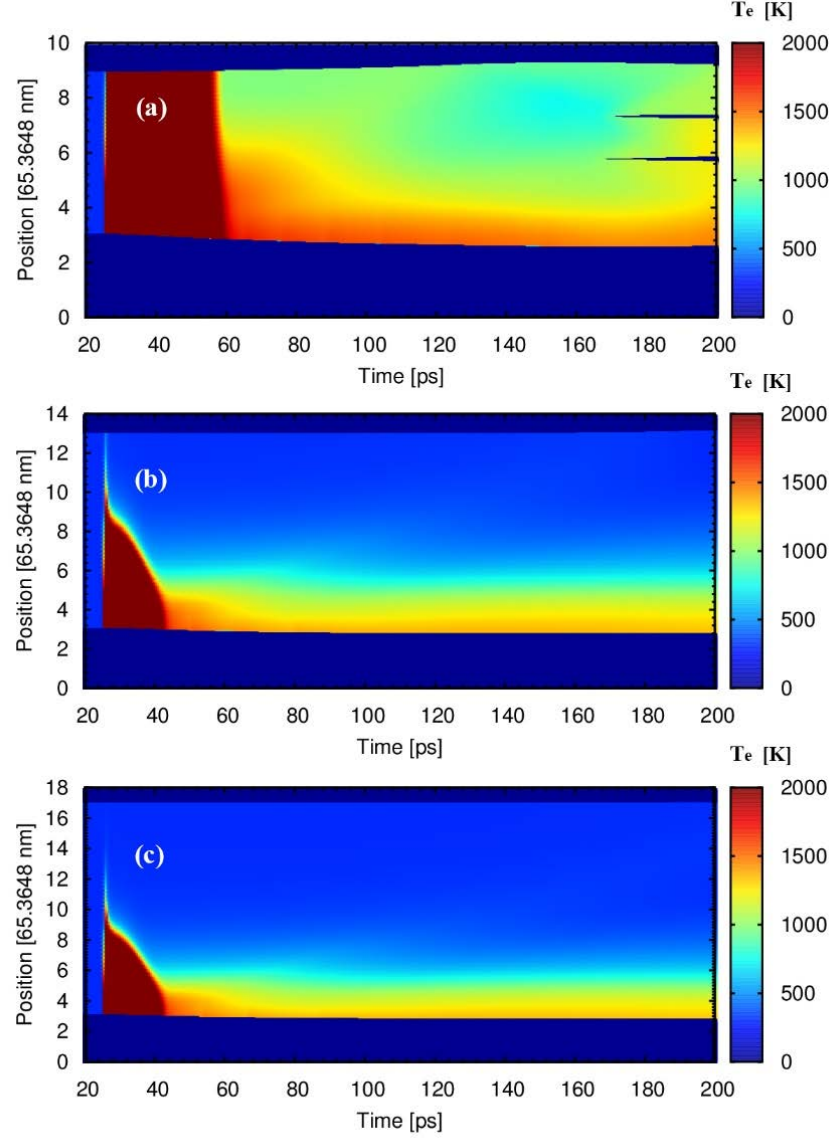


Fig. 2 The temporal and spatial distribution of electron temperature for the silver film thickness of (a) 392.1888 nm; (b) 653.6480 nm and (c) 915.1072 nm for $J_{abs} = 0.1 \text{ J/cm}^2$.

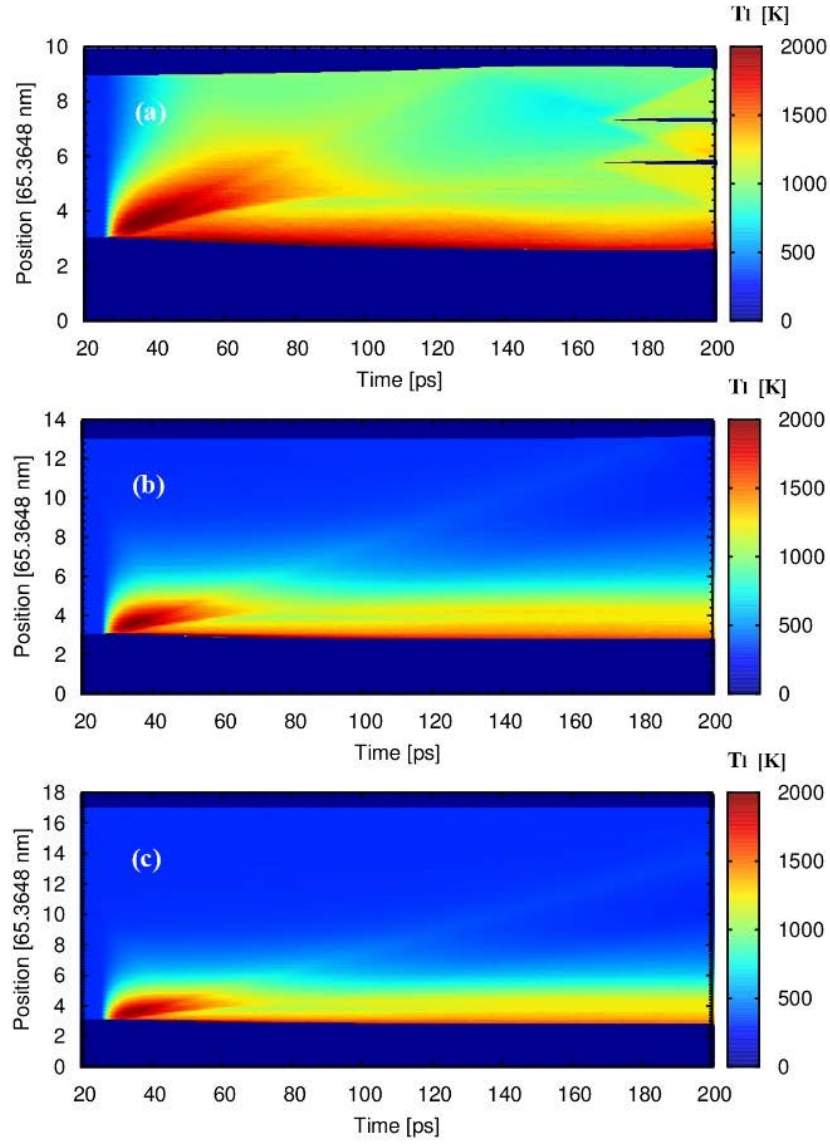


Fig. 3 The temporal and spatial distribution of lattice temperature for the silver film thickness of (a) 392.1888 nm; (b) 653.6480 nm and (c) 915.1072 nm for $J_{abs} = 0.1 \text{ J/cm}^2$.

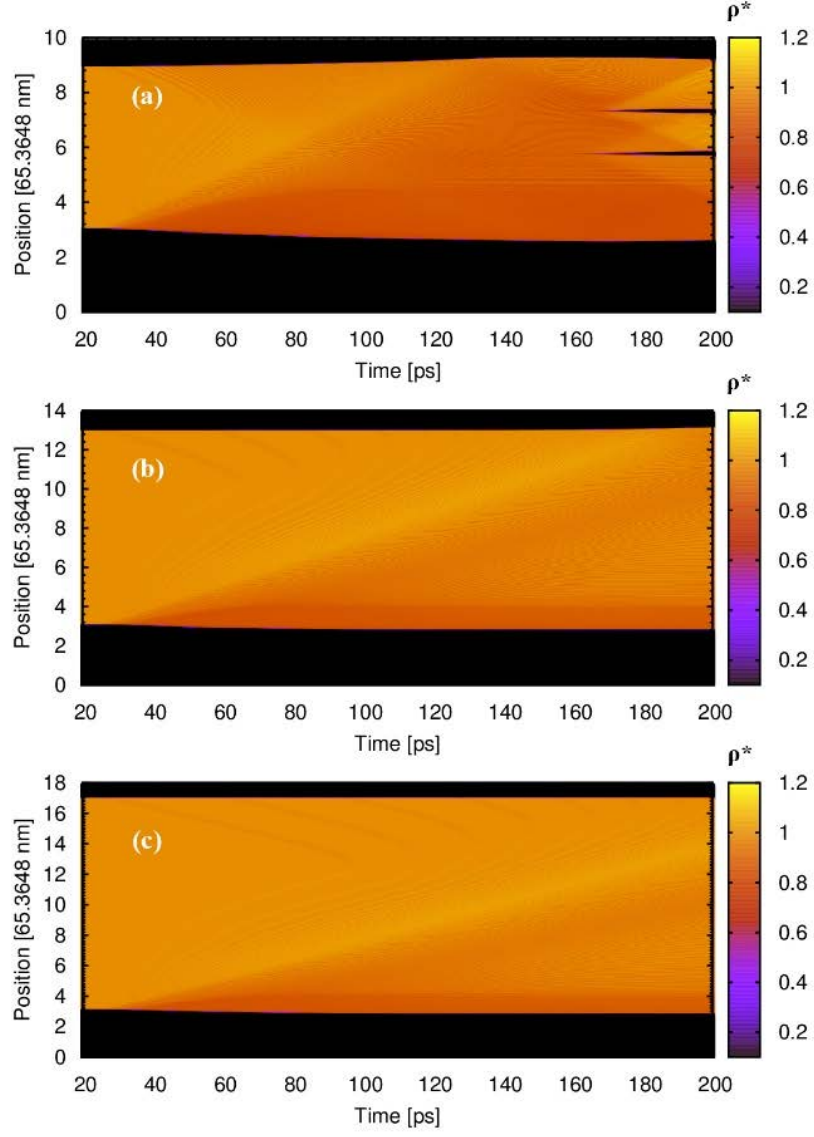


Fig. 4 The temporal and spatial distribution of normalized density for the silver film thickness of (a) 392.1888 nm; (b) 653.6480 nm and (c) 915.1072 nm for $J_{abs} = 0.1 \text{ J/cm}^2$.

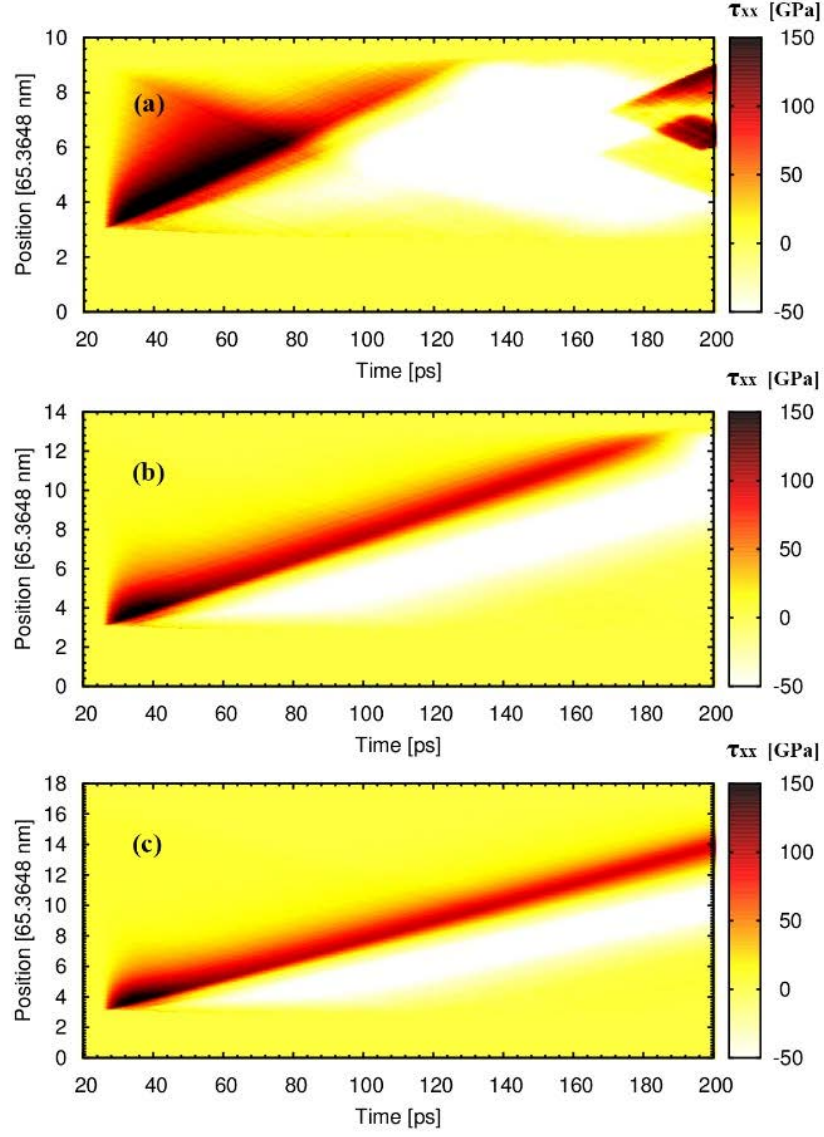


Fig. 5 The temporal and spatial distribution of thermal stress for the silver film thickness of (a) 392.1888 nm; (b) 653.6480 nm and (c) 915.1072 nm for $J_{abs} = 0.1 \text{ J/cm}^2$.

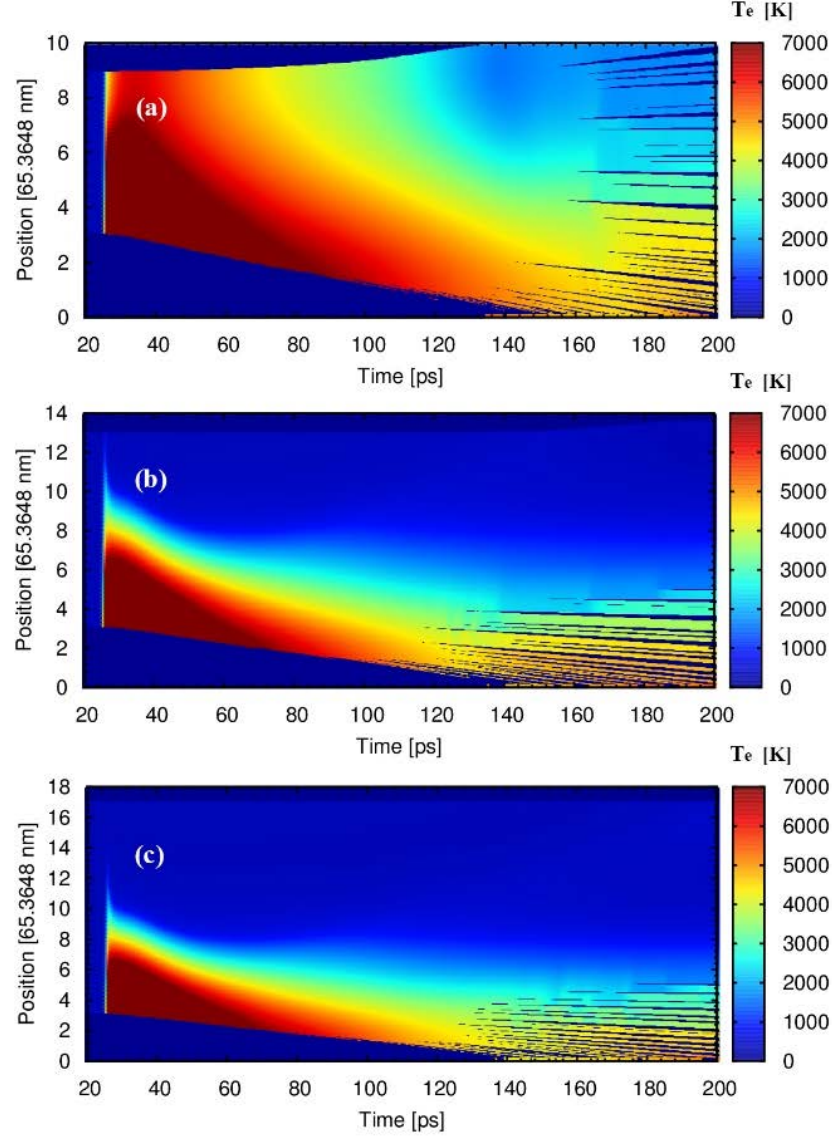


Fig. 6 The temporal and spatial distribution of electron temperature for the silver film thickness of (a) 392.1888 nm ; (b) 653.6480 nm and (c) 915.1072 nm for $J_{abs} = 0.3 \text{ J/cm}^2$.

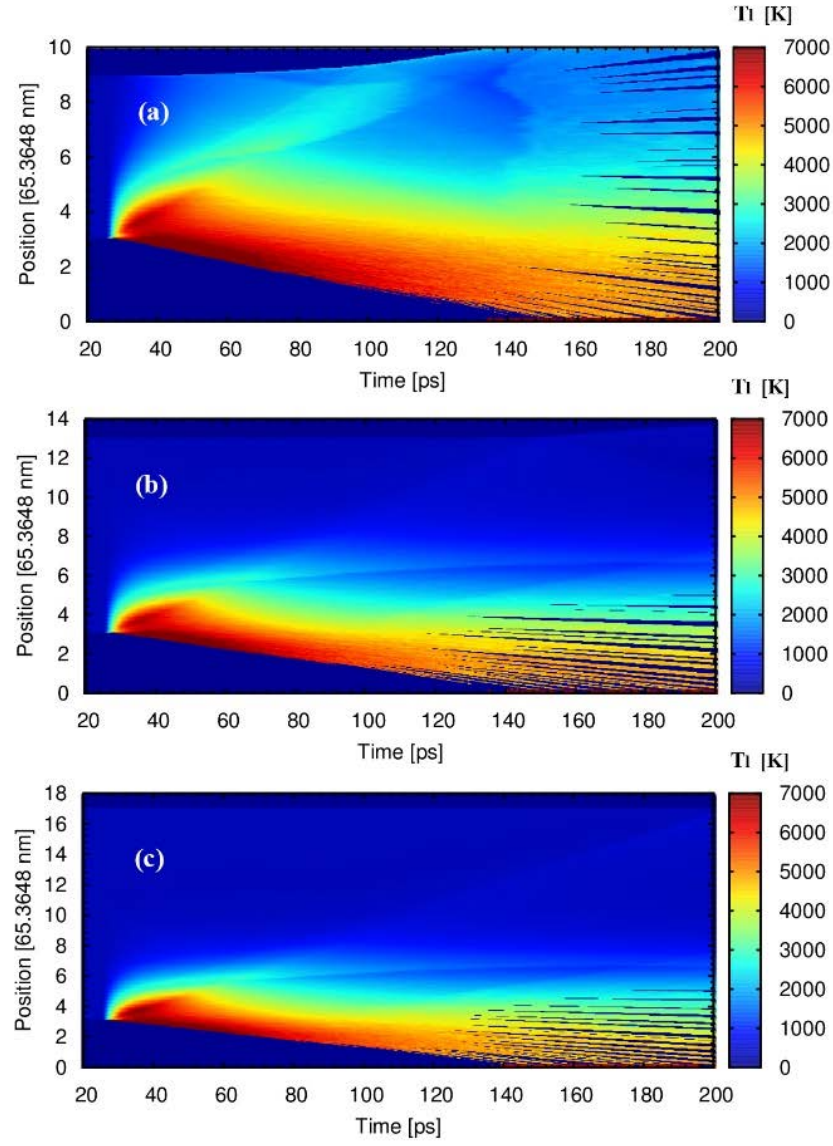


Fig. 7 The temporal and spatial distribution of lattice temperature for the silver film thickness of (a) 392.1888 nm; (b) 653.6480 nm and (c) 915.1072 nm for $J_{abs} = 0.3 \text{ J/cm}^2$.

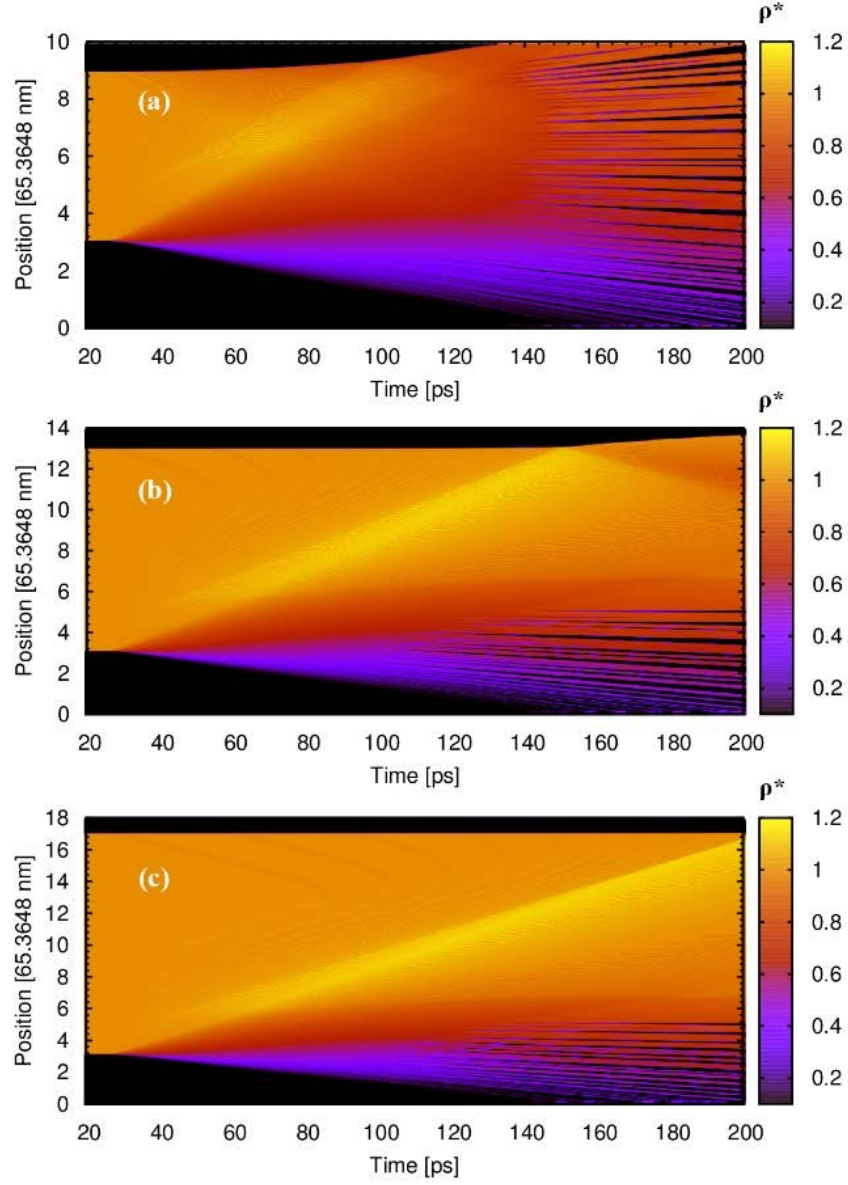


Fig. 8 The temporal and spatial distribution of normalized density for the silver film thickness of (a) 392.1888 nm; (b) 653.6480 nm and (c) 915.1072 nm for $J_{abs} = 0.3 \text{ J/cm}^2$.

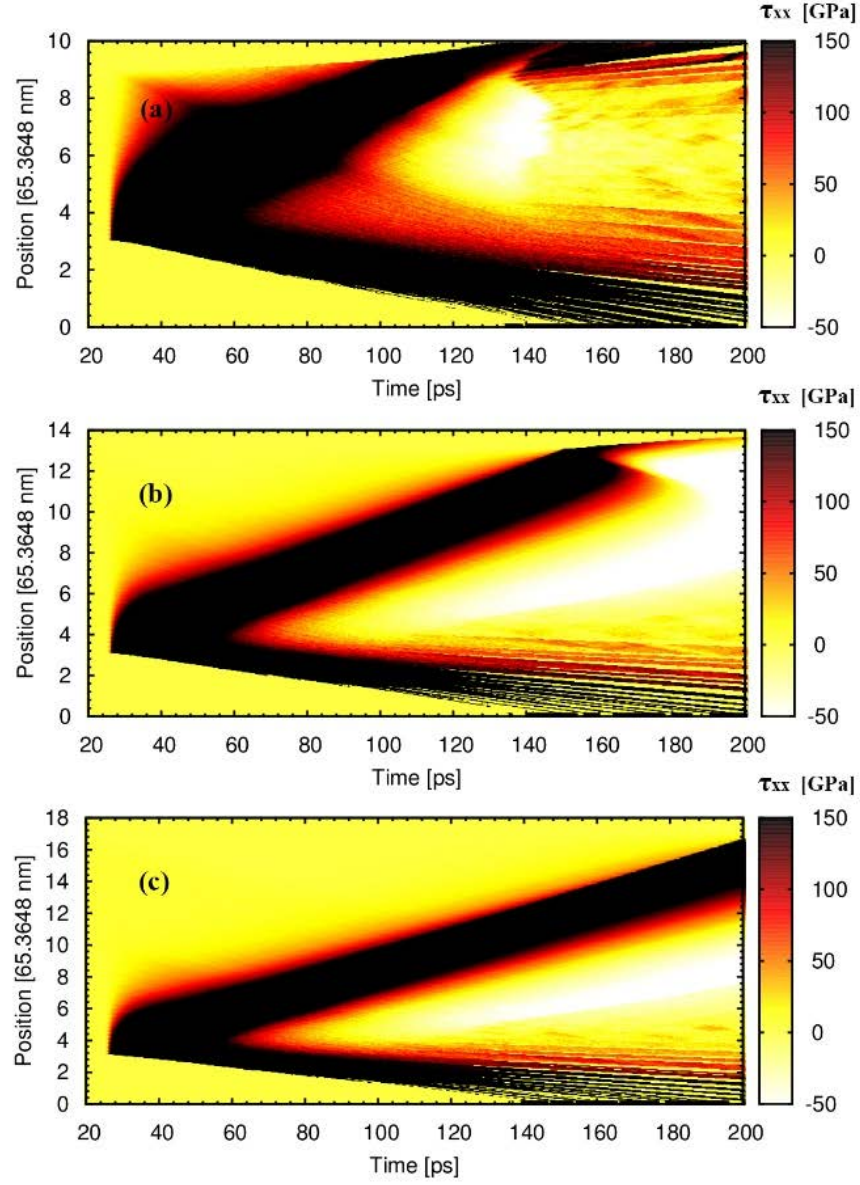


Fig. 9 The temporal and spatial distribution of thermal stress for the silver film thickness of (a) 392.1888 nm; (b) 653.6480 nm and (c) 915.1072 nm for $J_{abs} = 0.3 \text{ J/cm}^2$.